Clays and Clay Minerals, Vol. 58, No. 6, 783–791, 2010.

CLAY MINERALS IN SAPROLITE OVERLYING HYDROTHERMALLY ALTERED AND UNALTERED ROCKS, VERA EPITHERMAL GOLD DEPOSIT, AUSTRALIA

DAVID M. K. MURPHY* AND ROBERT J. GILKES

School of Earth and Environment (M087), The University of Western Australia, 35 Stirling Highway, Crawley, Western Australia 6009

Abstract—Differentiating clay minerals that formed in a supergene environment during deep chemical weathering from those that formed during hydrothermal alteration at higher temperatures associated with a mineralizing event is important in the exploration for epithermal Au deposits. The purpose of this study was to further elucidate this topic by comparing morphological and chemical properties of clay minerals in saprolite overlying epithermally altered bedrock at the Vera Au deposit, Queensland, Australia, with those of clay minerals in saprolite overlying bedrock adjacent to the epithermal alteration zone. X-ray diffraction (XRD) and analytical transmission electron microscopy (ATEM) investigations identified kaolinite, illite, and interstratified illite-smectite, together with quartz, Fe and Ti oxide minerals, and the sulfate minerals jarosite, gypsum, alunite, and natroalunite. Kaolinite crystals within the weathered argillic alteration zone proximal to the epithermal quartz vein are generally larger (up to 3 μm in diameter) and better formed (subhedral to euhedral) than crystals in saprolite distal to the hydrothermal alteration zone, in which smaller (mostly <1 μm), subhedral to anhedral crystals dominate. Energy-dispersive spectrometry (EDS) analysis of single crystals indicated that kaolinite within the alteration zone has an Al/Si ratio indistinguishable from reference kaolinite and has small Fe concentrations, whereas distal saprolitic kaolinite has smaller Al/Si and greater Fe/Si ratios, consistent with the formation of low-Fe kaolinite during hydrothermal alteration and higher-Fe kaolinite during weathering. Illite and interstratified illite-smectite (I-S) were distinguished from kaolinite by their morphology and greater K/Si and smaller Al/Si ratios. The Illite and I-S morphology ranged from thin irregular masses through lath-like crystals in hydrothermal samples to larger, irregularly shaped crystals. The Ca/Si and K/Si ratios of single crystals in Ca-saturated clay minerals were consistent with the I-S interstratification parameters determined from XRD patterns.

Key Words—Analytical Electron Microscopy, Clay Minerals, Epithermal Gold Deposit, Kaolinite, Weathering, X-ray Diffraction.

INTRODUCTION

The hydrothermal alteration systems associated with epithermal Au deposits are commonly larger than the deposits themselves, and hence form attractive exploration targets. However, recognizing these alteration systems in deeply weathered terrains is problematic because the clay-dominated portion of the alteration-mineral assemblage that survives weathering resembles the assemblage formed from chemical weathering of unaltered rock. The present study compared the clay minerals in weathered rock that had been altered by epithermal fluids during a pre-weathering epithermal Au-mineralizing event with clay minerals in adjacent weathered rock that had not been altered during the epithermal event, with a view to distinguishing weathered epithermally altered and unaltered rocks. Previous studies recognized differences in the morphology and composition of kaolinite in different environments. Large, well crystallized kaolinite occurs in epithermal and geothermal environments (Dill *et al*., 1997; Simpson *et al.*, 2001; Tillick *et al.*, 2001; Mas *et al*., 2003) and in saprolite underlying kaolin deposits (Varajão *et al*., 2001), whereas small crystals of disordered, Fe-substituted kaolinite occur in tropical soils (Herbillon *et al.*, 1976; St Pierre *et al*., 1992; Hart *et al.*, 2002, 2003). Both crystal morphology and composition were used by Dill *et al*. (1997) to distinguish hypogene kaolinite associated with argillic alteration in an epithermal setting from supergene kaolinite formed by weathering, the former being more ordered and containing less Fe and Ti. Such criteria to recognize relict argillic alteration systems in deeply weathered terrains have important implications for exploration for epithermal Au deposits.

Samples were collected from saprolite at the Vera deposit, located within the Carboniferous Vera Nancy low-sulfidation epithermal Au system in northeast Queensland, Australia (20º33′S, 146º28′E). Quartz-vein-hosted Au mineralization occurs in hydrothermally altered andesite (Richards *et al.*, 1998; Mustard *et al.*, 2003). Hydrothermal alteration of wallrocks, which occurred during the epithermal event, is zoned from an inner 15–60 m thick zone of highly siliceous and pyritic rock adjacent to the vein, through an illite, kaolinite, Fe-carbonate, and pyrite-rich argillic zone up to 175 m

* E-mail address of corresponding author:
davidmkmurphy@gmail.com
DOI: 10.1346/CCMN.2010.0580606

thick. The epithermal alteration system is located within a regionally extensive background propylitic (albite-calcite-chlorite-quartz) alteration zone that is probably unrelated to the epithermal mineralization (Mustard *et al.*, 2003; Stanley *et al.*, 2003).

Subsequent to propylitic and epithermal alteration, the deposit and surrounding rocks experienced deep lateritic weathering during the Tertiary period (Butt, 1989). The study area provides the opportunity to compare saprolite derived from epithermally altered rocks with saprolite from the same andesite precursor which experienced the regional propylitic alteration only.

MATERIALS AND METHODS

Ten samples representing material from within, peripheral to, and distal from the epithermal alteration system were examined (Figure 1). These are referred to hereafter as 'epithermal,' 'transitional,' and 'background,' and are prefixed with 'E,' 'T,' and 'B,' respectively. Epithermally altered material was collected from vertical drill hole JMR 1768 at 10, 30, and 50 m depth (samples E10, E30, and E50). Propylitic material from the periphery of the epithermal alteration system (transitional saprolite) was collected from inclined drill hole JMRD 1850 at 15, 35, and 55 m down-hole depth, corresponding to 13, 31, and 50 m vertical depth (samples T15, T35, and T55). Background propylitic material was collected from JMRD 2576 at 15, 35, 55, and 75 m down-hole depth (13, 31, 50, and 68 m vertical depth; samples B15, B35, B55, and B75). All samples were saprolite except the uppermost sample in JMRD2576 (sample B15), which comprised locally transported sediment (Southern Cross Formation), derived from the same andesitic precursor, and reworked during a Tertiary erosional-local redepositional event. Clay-fraction (nominally <2 μm equivalent spherical diameter) samples were separated by sedimentation after dispersion in de-ionized water from material collected during reverse circulation drilling. Samples of Ward's kaolinite (Macon, Georgia, USA) and Ward's muscovite were used as reference materials.

X-ray diffraction scans were collected using monochromatic CuKα radiation on a Philips PW 3020 diffractometer, operating at 50 kV and 20 mA. Random powder samples were scanned at 0.02º2θ/s and Ca-exchanged, ethylene glycol solvated, basally oriented clay samples at 0.005º2θ/s. Kaolinite crystal thickness was calculated from the 001 reflection using the Scherrer equation (Klug and Alexander, 1974). Illite-smectite interstratification parameters were determined from Δ2θ diagrams (Watanabe, 1981; Inoue and Utada, 1983; Moore and Reynolds, 1997).

The TEM analysis was undertaken on dispersed samples. Fe (oxyhydr)oxide minerals were removed from clay-fraction samples by bicarbonate-buffered Na dithionite-citrate extraction (Mehra and Jackson, 1958). The purified clay was exchanged with $CaCl_2$, washed with de-ionized water, and allowed to air dry. A highly diluted suspension of this material was made with de-ionized water. After ultrasonic dispersal, a drop of suspension was placed, without delay, on a 3 mm carbon-coated Cu grid and allowed to dry.

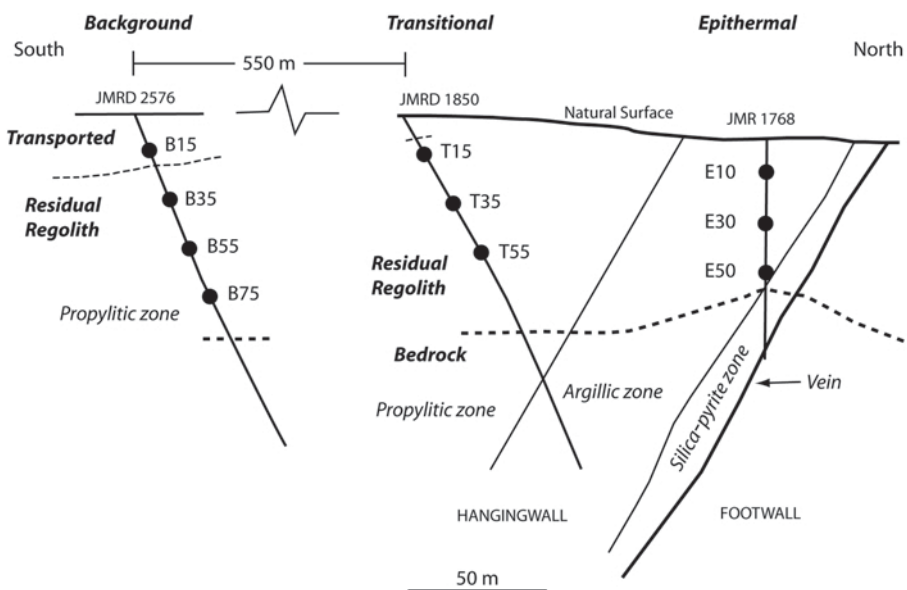

Figure 1. Cross section showing the locations of the samples subjected to analysis by TEM with respect to regolith position and alteration zone.

Bright-field images and electron diffraction patterns were obtained using a JEOL 2000 FX TEM at 80 keV. Additional images and all microanalyses were acquired on a JEOL 3000 F Field Emission TEM at 300 keV. Individual crystals were analyzed with a defocused (400−500 nm approximate diameter) probe for 100 live seconds, using an Oxford Instruments INCA 200 energy dispersive spectrometry (EDS) system. X-rays were collected in 10 eV bins from 0 to 10 keV. The beam current of 2 nA generated in excess of 10,000 counts s^{-1} on thick kaolinite crystals. Where crystals were smaller than the beam diameter, the beam was incident on both the crystal and the surrounding carbon film. In some cases several crystals fell within the beam. Although these analyses reported greater total X-ray counts because the beam was incident on more kaolinite, each crystal was subject to the same current density, and so the same potential for heat-induced damage, as well-separated single crystals on the carbon film.

An estimate of the size distribution of kaolinite crystals was made from low-magnification images of dispersed crystals using methods described by Varajão *et al*. (2001). The basal areas of 426 crystals from five images were measured using the particle analysis functions of NIH *ImageJ*™ software. As most crystals were approximately equidimensional, crystal diameters were estimated from circles with the same areas.

Intensity ratios for EDS spectra were calculated from background-subtracted Al, Si, K, and Fe peak heights. Backgrounds for Al and Si were estimated from a linear interpolation between counts at 1.0 and 1.9 keV, the left end being positioned to avoid other peak interferences. The K and Fe peaks appeared free from interference. A CaKα peak (3.69 keV) was observed for some Ca-saturated I-S. Counts due to the overlapping KKβ peak (3.59 keV) were removed using the relationship between the heights of the KKα peak and the height of the shoulder of the KKβ peak at 3.69 keV (the location of the CaKα peak) in Ca-free samples. Visual examination of spectra of high-purity kaolinite generating large Si and Al count rates showed no evidence of Si + Si, Al + Al, or Si + Al sum peaks. Analyses of blank carbon films confirmed that the grids were uncontaminated and that no significant spurious X-rays from the instrument were recorded.

Given the fragility of kaolinite in the electron beam (Robertson and Eggleton, 1991), and differential volatility of Al and Si in kaolinite during beam-induced heating (Ma *et al.*, 1998), sequential analysis tests with a range of beam diameters were undertaken to determine the minimum beam size that did not cause significant changes in Al/Si ratio during the course of analysis. These tests involved collection of ten immediately consecutive measurements for 20 live s duration from each of five sites on a large crystal of reference kaolinite, each one with a different probe size. The intervening manual acquisition restart time was <1 s, and the delay between positioning the electron beam and commencing acquisition of the first spectrum was ~5 s. The resulting spectra estimated the X-ray yield for the (live) time periods (ignoring initial positioning time) 0−20 s, 20−40 s, out to 180−200 s, corresponding to a total of ~240 s of incident beam time. All probes caused visible damage to the sample.

An inverse relationship was found between Al/Si intensity ratio and probe diameter. The ratios for the smallest probe size (70 nm) were not only considerably smaller than those for all the other probe sizes (Al/Si $\approx$ 0.7), but this ratio was achieved after <20 s, indicating that small probes induce damage in very short time periods. The Al/Si ratio for intermediate probe sizes of 160−200 nm decreased to ~0.9 over the analysis period, whereas the ratio for the largest probes (400−500 nm) remained close to unity and showed no systematic variation during analysis.

Dispersed clay mineral crystals approximate the properties of thin films for electron optical elemental analysis. Therefore, atomic number, X-ray absorption, and fluorescence (ZAF) effects are insignificant, and relative elemental concentrations are directly proportional to relative X-ray intensities (Cliff and Lorimer, 1975). In the present study, intensities were ratioed against Si (Lorimer and Cliff, 1976) and, following Ma *et al.* (1998), the proportionality (k) factors relating intensity to compositional ratios were determined for molar rather than weight ratios. Effective k factors for Al/Si were determined from both muscovite and kaolinite spectra, and those for K/Si and Fe/Si from muscovite spectra, using compositional data obtained from X-ray fluorescence analyses of bulk samples of the reference materials at a commercial laboratory. Effective k factors for Al/Si and K/Si were close to unity, and for Fe/Si the factor was 1.25, indicating that, for these elements under these analytical conditions, intensity ratios approximate atomic ratios.

Uncertainty in element ratios arises from counting statistics and this is expressed as the variability of repeat analyses of the same crystal. The bright-field emission source resulted in high X-ray counts, particularly for thick crystals, and hence counting errors, which are proportional to $\sqrt{n}$, are small relative to the total count n. Although some variation was noted between duplicate analyses on the same crystal, precision was deemed adequate to resolve significant compositional variations.

RESULTS AND DISCUSSION

The XRD patterns of random powder samples showed that saprolite is dominated by quartz, kaolinite, illite, I-S, smectite, and goethite, with lesser amounts of anatase, albite, and the sulfate minerals jarosite, alunite, natroalunite, and gypsum, whereas the Southern Cross Formation is dominated by quartz, kaolinite, and goethite. Kaolinite is the most abundant clay mineral in almost all samples.

Illite and I-S are present within 50−100 m of the epithermal vein, whereas discrete smectite and small amounts of illite occur distal to the alteration zone. For basally oriented clay-fraction samples, superlattice reflections and the spacing of diffraction peaks in the 6−10º2θ range indicate that I-S in samples E10 and E30 exhibit R1 nearest-neighbor ordering, whereas I-S in E50, T35, and T55 is more illitic and shows long-range R3 ordering (Figure 2). Narrower diffraction-peak widths indicate the presence of thicker kaolinite crystals in epithermal samples than in background samples. Transitional samples, of propylitic material immediately outside the alteration zone, contain kaolinite intermediate in thickness between that of epithermal and background materials.

Crystals of kaolinite, illite or I-S, and a Ti oxide mineral were observed by TEM in all samples (Figure 3). Some samples also contain quartz and jarosite. Although smectite was identified by X-ray diffraction in background samples, smectite crystals with a distinct morphology were not recognized in the TEM. Fe (oxyhydr)oxide minerals were also not recognized in the TEM, indicating that the samples had been purified successfully.

Most kaolinite crystals are approximately equidimensional in the (001) plane, although elongate (length:width > 2) crystals occur also. Kaolinite crystals in epithermal samples are mostly subhedral to euhedral (Figure 3a,b), whereas transitional and background samples contain smaller and less regularly shaped kaolinite crystals (Figure 3c,d). Rare tubular Al-Si crystals are probably halloysite (Figure 3c).

The quantification of kaolinite crystal size made from low-magnification images showed that sizes ranged from <100 nm to >3 μm equivalent spherical diameter (Figure 4). Samples B15 and T15 showed the smallest modes (50−100 μm), larger crystals occurred in B35 and T35 (mode 100−150 nm), and the largest were found in E10. The size distribution recorded for E10 is bimodal, with a smaller mode approximately equal to the modes for the T and B samples, and a much larger mode of 800 nm.

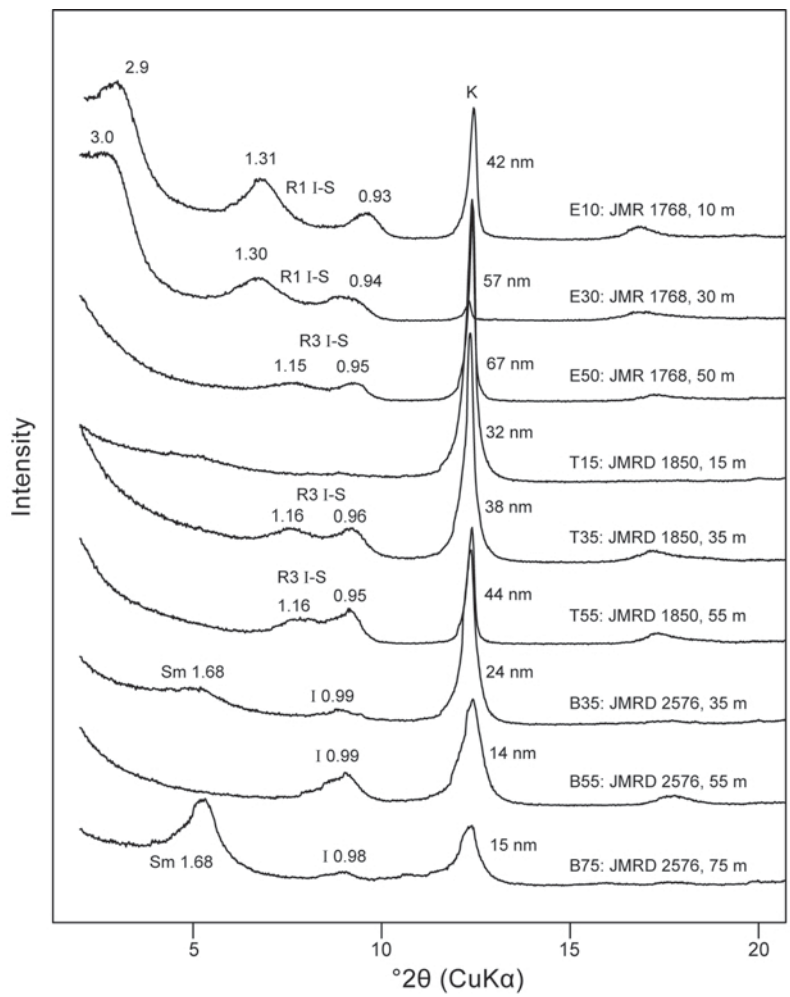

Figure 2. XRD patterns for Ca-saturated and ethylene-glycol solvated clay-fraction samples. K = kaolinite, with Scherrer thickness indicated; I = illite; Sm = smectite; and I-S = interstratified illite-smectite, with *d* spacings (nm) indicated. R is the Reichweite factor.

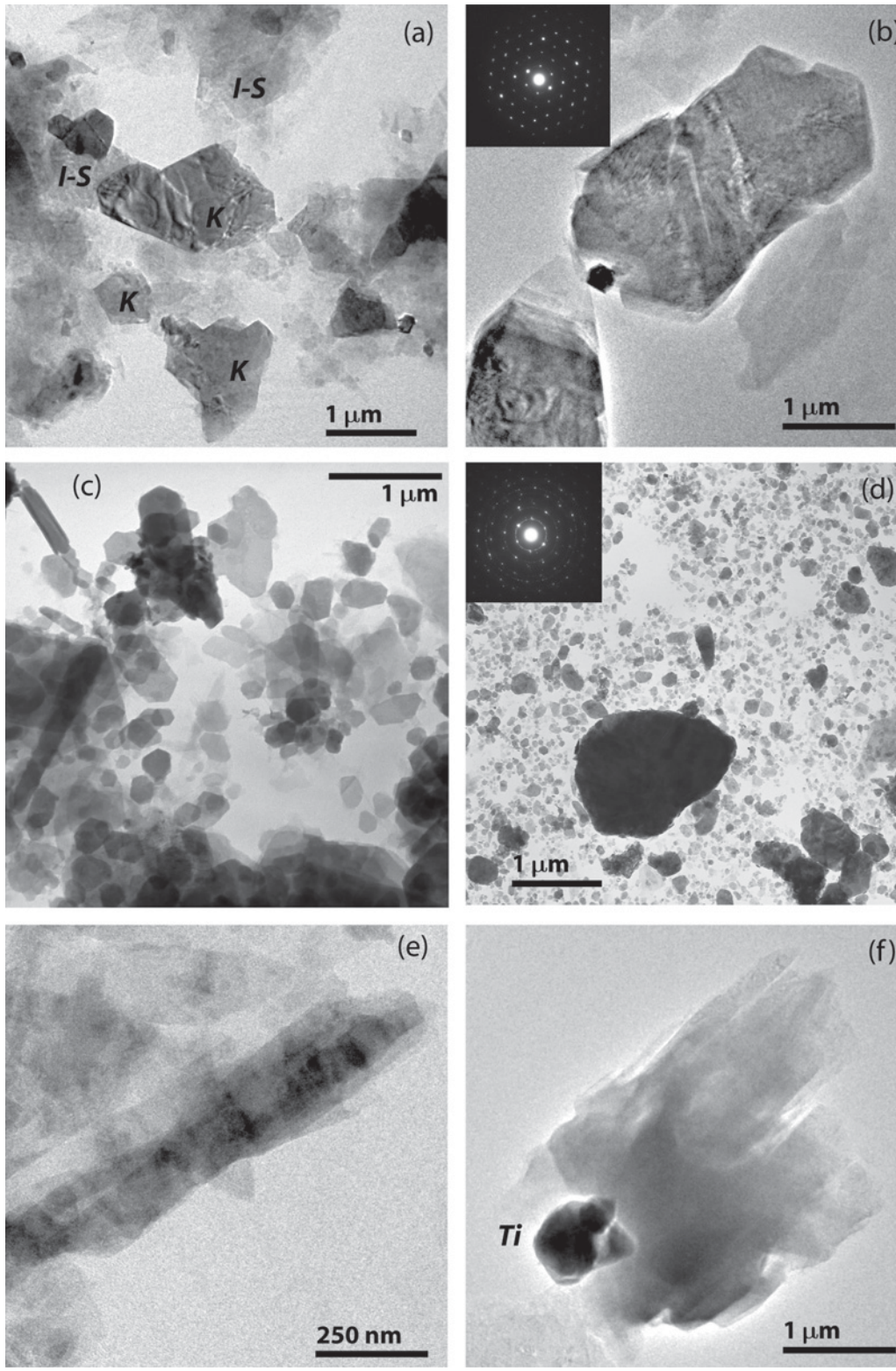

Figure 3. Bright-field TEM images of clay-mineral particles from regolith samples. Images a, b, e, and f were obtained at 300 keV; images c and d were obtained at 80 keV. (a) E50 Euhedral kaolinite and thin plates of I-S. (b) E30 Euhedral kaolinite. The electron diffraction pattern is for the crystal in the center of the field of view. (c) B35 Hexagonal kaolinite and tubular halloysite crystals. (d) B15 Kaolinite. The electron diffraction pattern is for the large crystal. (e) E30 Lath-shaped I-S. (f) E30 Illite and Ti oxide (Ti).

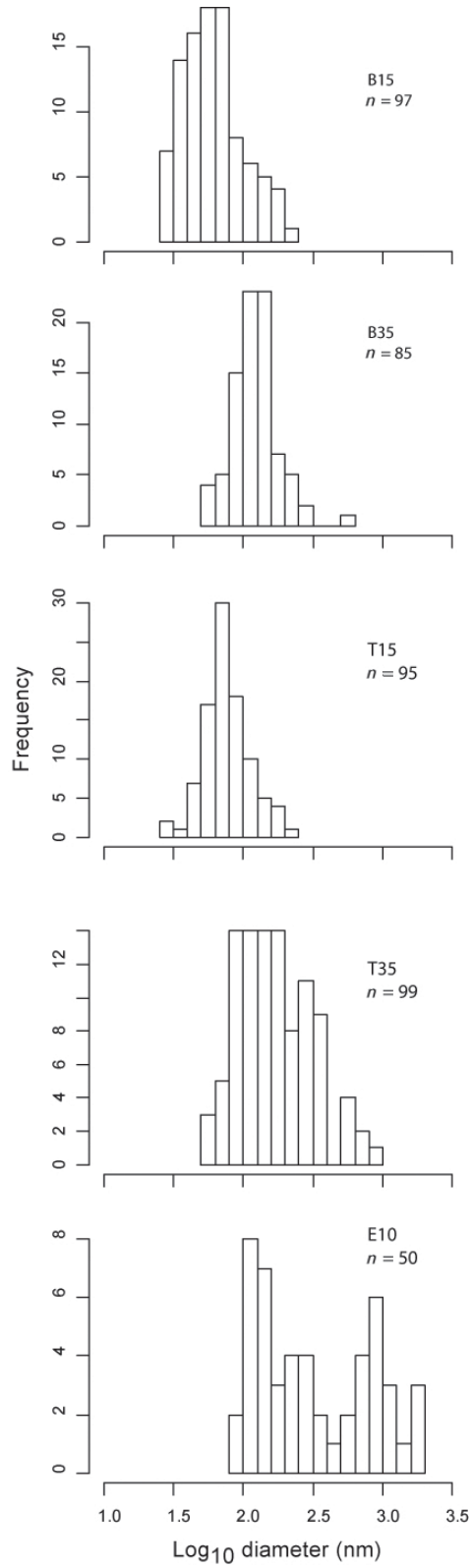

Figure 4. Histograms showing the frequency of occurrence of kaolinite crystal diameters, based on areas measured from five images.

The larger crystals in the epithermal samples are generally thicker, as indicated both by their dark appearance in TEM images and by CSD (001) measurements from XRD patterns. They make up most of the kaolinite mass in these samples.

Illite or interstratified I-S occur in all samples as thin, irregularly shaped, low-contrast particles (Figure 3a) that generate small X-ray counts during microanalysis. Lath-shaped I-S occurs in epithermal samples (Figure 3e), and larger irregular crystallites of illite occur in both epithermal and transitional samples (Figure 3f).

A diagram of intensity ratios for K/Si *vs.* Al/Si distinguishes single crystals of kaolinite from illite and I-S (Figure 5), although some analyses of kaolinite showing elevated K/Si may reflect particles of mixed mineralogy. The Al/Si intensity ratio for kaolinite crystals in transitional and background samples ranges from 0.72 to 0.98 (mean 0.87, standard deviation 0.07), and from 0.87 to 1.07 (mean 0.97, standard deviation 0.04) for epithermal samples. The Al/Si ratio for the reference kaolinite ranges from 0.94 to 1.06 (mean 0.99, standard deviation 0.05), which essentially coincides with the range for the epithermal kaolinite. The K/Si ratio for kaolinite is <0.05 for most samples, and is unrelated to the location of the sample with respect to the alteration system. The K/Si ratio of the reference kaolinite is <0.01.

Kaolinite from epithermal samples is distinguished from background and transitional samples by a more restricted and generally smaller range of values of the Fe/Si ratio (Figure 6). This ratio is <0.01 for most epithermal sample kaolinite crystals, whereas for transitional and background kaolinite, values range up to 0.05.

The smaller than ideal Al/Si and non-zero Fe/Si ratios for many analyses of kaolinite crystals from transitional and background samples probably indicates the occurrence of Fe substitution for Al in octahedral sites; however, this limited substitution of Fe for Al does not fully explain the low Al/Si ratio (Figure 6). The Al/Si ratio may also be reduced by the presence of low-Al layers, amorphous Si, or the loss of Al during analysis by sputtering or diffusion. Pyrophyllitic layers (Al/Si = 0.5), which have been reported to occur at the surface of poorly ordered regolith kaolinite particles by Ma and Eggleton (1998), would significantly reduce the overall Al/Si ratio for thin crystals. A ratio of 0.86, typical of background kaolinite, could arise from a 14 nm thick particle (CSD measurement from X-ray diffraction profile; Figure 2) with two pyrophyllite layers on each side. It would contain 20 layers of kaolinite and four layers of pyrophyllite, giving a bulk ratio of $0.86([20 \times 4 + 4 \times 4])/[(20 \times 4 + 4 \times 8)]$. As the k factor is close to unity, this molar ratio is effectively the same as the expected intensity ratio. Such a particle would give a broad kaolinite XRD basal reflection as is observed and no reflection for pyrophyllite. A reduction in the Al/Si

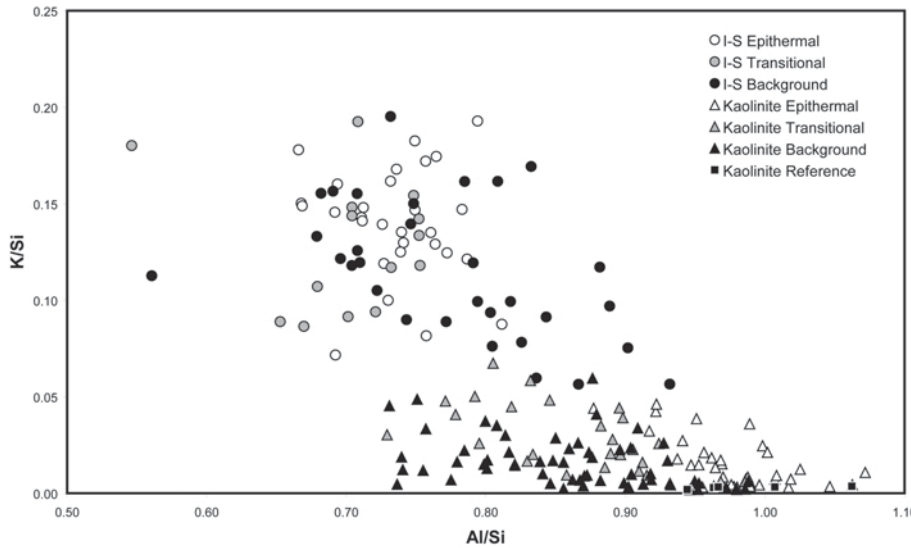

Figure 5. Scatterplot of EDS intensity ratio for kaolinite and illitic (illite and I-S) clay minerals from epithermal, transitional, and background samples.

ratio would also result from the presence of excess Si (*e.g.* as in the Dorset ball clay studied by Jepson and Rowse (1975)), possibly as amorphous silica attached to kaolinite crystals. This would cause data points to plot closer to the origin in Figures 5 and 6. Alternatively, the small Al/Si ratios may result from the diffusion or sputtering of Al atoms in the defocussed electron beam. Although the large beam diameters used did not induce a decrease in Al/Si ratio during analysis for the well ordered Georgia kaolinite, Vera kaolinite crystals may have lost Al during analysis, as small disordered crystals are commonly less stable at higher temperature and dehydroxylate at lower temperatures (Hart *et al.*, 2002). Small ratios are unlikely to arise from the inadvertent incorporation of illite in kaolinite aggregates because most samples plot below the mixing line between kaolinite and illite (Figure 5). Although the cause(s) of the variation in values of the Al/Si ratio shown by T and B samples has not been resolved, it appears to be a characteristic of the material rather than an experimental artifact.

Two kaolinite morphologies were identified in the Southern Cross Formation sediments (B15; Figure 3d). Larger crystals, although anhedral, have large Al/Si and small Fe/Si ratios, whereas small crystals are relatively Al deficient and more ferruginous. The electron diffrac-

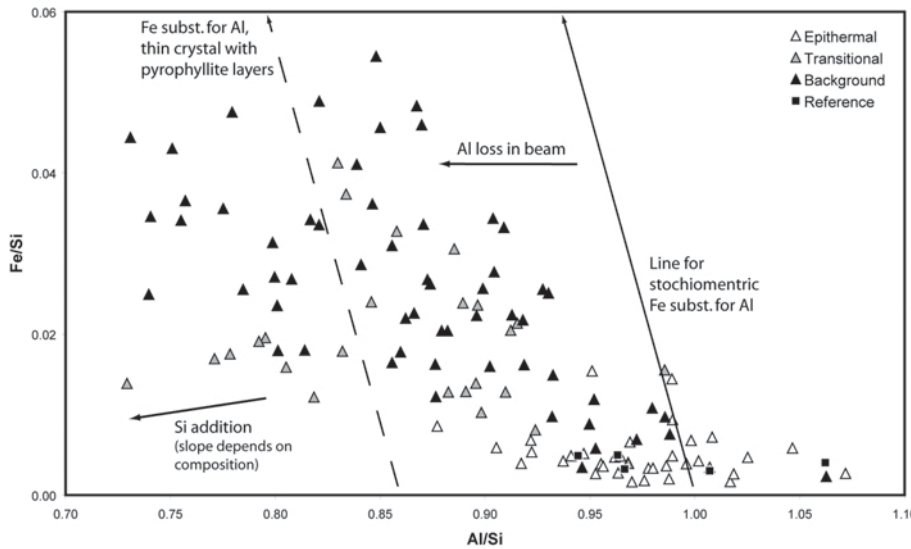

Figure 6. Scatterplot of intensity ratios of Fe/Si *vs*. Al/Si for EDS analyses of kaolinite. Arrows indicate the expected trends of the processes indicated (see text).

tion pattern consisting of sharp reflections on a regular hexagonal net indicates that the large particle in Figure 3d is a single crystal, and not an aggregate of small crystals. The coincident weak ring pattern represents the random arrangement of many small crystals visible beneath and/or upon and adjacent to the large crystal. This association of large and small crystals may reflect the physical mixing of epithermal and saprolitic kaolinites in the Tertiary sediment.

Analyses of illite and I-S crystals (Figure 5) revealed values of the Al/Si ratio between 0.50 and 0.95 (mean 0.75), with values being mostly 0.65−0.85, except for some illite from background samples in which the Al/Si ratio approaches unity. The K/Si ratio ranges from 0.05 to 0.2 (mean 0.13). The Al/Si and K/Si ratios for the muscovite reference material analyses averaged 0.83 and 0.29, respectively, which is consistent with the greater values of the Al/Si and K/Si for muscovite relative to illite (Środoń and Eberl, 1984). Values of the Fe/Si ratio for illite and I-S range from ~0.01 to 0.04, and values for epithermal samples are mostly smaller than values from T and B samples.

Ca peaks significantly above background were present in spectra for 22 of the 74 analyses of Ca-saturated illite and I-S. Of these, 16 are from the R1 I-S-bearing epithermal samples E10 and E30. The presence of Ca peaks indicates the greater smectite content, and presumably larger cation exchange capacity, of the R1 crystals relative to R3 I-S and illite. The Ca/Si and K/Si intensity ratios for individual crystals are comparable with molar ratios calculated for structures consisting of various mixtures of illite (I) and Ca-beidellite (S). Ratios for most epithermal samples plot close to the modeled ratios for structures with between 60 and 80% illite layers, which is consistent with estimates of composition from XRD patterns.

The precursor of the R1 I-S in the epithermal samples may have been illite that formed during the epithermal alteration event. This illite may have been altered to I-S by reaction with groundwater made acidic by pyrite oxidation during weathering (Murphy, 2009), in a process analogous to the early stages of the alteration of an illtic underclay close to an acid-generating coal seam described by Rimmer and Eberl (1982).

CONCLUSIONS

The present study shows that both the morphology and the composition of kaolinite crystals discriminates weathered material that had been altered during an epithermal Au-mineralizing event from weathered material that had experienced only a regional propylitic event.

Kaolinite is the dominant clay mineral present in the regolith. Kaolinite crystals tend to be smaller in saprolite derived from background and transitional rocks and larger in saprolite on the epithermal alteration zone. Kaolinite from saprolite in the epithermal alteration zone occurs as both large and small crystals. The smaller crystals are similar in size to those from the background and transitional zones. However, both the large and small crystal populations have similar chemical compositions.

Analysis by EDS of kaolinite crystals showed consistently larger values for the Al/Si ratio and smaller values of the Fe/Si ratio for samples from the epithermal alteration zones than for samples from outside this zone. Kaolinite from the epithermal alteration zone resembled the reference Macon kaolinite in having an approximately ideal composition. The reason for the small value of the Al/Si ratio determined for kaolinite in background samples is unknown, but is not a consequence of their much smaller size.

The larger and more euhedral morphologies and the greater and nearly ideal Al/Si and smaller Fe/Si ratios of kaolinite from epithermal samples are consistent with its formation at elevated temperature during epithermal activity. The relatively small range in values of Al/Si and Fe/Si suggest that little, if any, of this kaolinite was formed during lateritic weathering of the epithermal bedrock assemblage. This bedrock assemblage comprises illite, kaolinite, pyrite, Fe carbonate, and quartz. Of these, the only mineral that could weather to kaolinite is illite; however, illite occurs through the entire regolith and no kaolinite was identified that is chemically distinct from the large euhedral crystals inferred to be of epithermal origin. In contrast, the smaller, less aluminous and more ferruginous kaolinite crystals in propylitic rocks probably formed from hydrolysis of albite (and perhaps other rock-forming and clay minerals) during weathering at ambient temperature. The greater Fe content of the weathering-product kaolinite represents Fe within the kaolinite lattice (Weaver *et al.*, 1967; Jepson and Rowse, 1975; Herbillon *et al.*, 1976; Gualtieri *et al.*, 2000), and was incorporated during kaolinite neoformation during lateritic weathering.

No samples of kaolinite from unweathered argillically altered rock were available for the present study. A comparison of the morphology and chemical composition of such crystals with their equivalents from the regolith would provide valuable information, and is a goal of future research.

All samples contain illite or I-S. Lath-shaped I-S crystals and most I-S crystals that contain sufficient interstratified smectite to generate a Ca response during EDS analysis occur in epithermal samples in which I-S exhibits R1 interstratification. The greater smectite content in I-S from these epithermal samples is attributed to alteration of epithermal illite during weathering of the bedrock argillic alteration assemblage.

ACKNOWLEDGMENTS

This study was carried out as part of the first author's PhD research at the University of Western Australia. Newmont Asia Pacific, Ltd., is thanked for financial and

logistic assistance. The TEM investigations were carried out using facilities at the Centre for Microscopy, Characterization and Analysis, The University of Western Australia, which are supported by University, State, and Federal Government funding. The assistance of Dr Martin Saunders and Mr Steve Parry (TEM analysis) and Dr Janet Muhling (microanalysis) is gratefully acknowledged. The manuscript was improved by helpful comments from the editors and an anonymous reviewer.

REFERENCES

Butt, C.R.M. (1989) Geomorphology and climate history – keys to understanding geochemical dispersion in deeply weathered terrains, exemplified by gold. Pp. 323–334 in: *Proceedings of Exploration '87*. Third Decennial International Conference on Geophysical and Geochemical Exploration for Minerals and Groundwater (G.D. Garland, editor). Special Volume **3**, Ontario Geological Survey, Canada.

Cliff, G. and Lorimer, G.W. (1975) The quantitative analysis of thin specimens. *Journal of Microscopy*, **103**, 203–207.

Dill, H.G., Bosse, H.-R., Henning, K.-H., Fricke, A., and Ahrend, H. (1997) Mineralogical and chemical variations in hypogene and supergene kaolin deposits in a mobile fold belt – the Central Andes of northwestern Peru. *Mineralium Deposita*, **32**, 149–163.

Gualtieri, A.F., Moen, A., and Nicholson, D.G. (2000) XANES study of the local environment of iron in natural kaolinites. *European Journal of Mineralogy*, **12**, 17–23.

Hart, R.D., Gilkes, R.J., Siradz, S., and Singh, B. (2002) The nature of soil kaolins from Indonesia and Western Australia. *Clays and Clay Minerals*, **50**, 198–207.

Hart, R.D., Wiriyakitnateekul, W., and Gilkes, R.J. (2003) Properties of clay minerals from Thailand. *Clay Minerals* **38**, 71–94.

Herbillon, A.J., Mestagh, M.M., Vielvoye, L., and Derouane, E. (1976) Iron in kaolinite with special reference to kaolinite from tropical soils. *Clay Minerals*, **11**, 201–220.

Inoue, A. and Utada, M. (1983) Further investigations of a conversion series of dioctahedral micas/smectites in the Shinzan hydrothermal alteration area, northeastern Japan. *Clays and Clay Minerals*, **35**, 111–120.

Jepson, W.B. and Rowse, J.B. (1975) The composition of kaolinite – an electron microscope microprobe study. *Clays and Clay Minerals*, **23**, 310–317.

Klug, H.P. and Alexander, L.E. (1974) *X-ray diffraction Procedures for Polycrystalline and Amorphous Materials.* John Wiley and Sons Inc., New York, London.

Lorimer, G.W. and Cliff, G. (1976) Analytical electron microscopy of minerals. Pp. 506–519 in: *Electron Microscopy in Mineralogy* (H.E. Wenk, editor). Springer, Berlin.

Ma, C. and Eggleton, R.A. (1998) Surface layer types of kaolinite: a high-resolution transmission electron microscope study. *Clays and Clay Minerals*, **47**, 181–191.

Ma, C., Fitzgerald, J.D., Eggleton, R.A., and Llewellen, D.J. (1998) Analytical electron microscopy in clays and other phyllosilicates: loss of elements from a 90-nm stationary beam of 300-keV electrons. *Clays and Clay Minerals*, **46**, 301–316.

Mas, A., Patrier, P., Beaufort, D., and Genter, A. (2003) Clay-mineral signatures of fossil and active hydrothermal circulations in the geothermal system of the Lamentin Plain, Martinique. *Journal of Volcanology and Geothermal Research*, **124**, 195–218.

Mehra, O.P. and Jackson, M.L. (1958) Iron oxide removal from soils and clays by a dithionite-citrate system buffered with sodium bicarbonate. *Clays and Clay Minerals*, **7**, 317–327.

Moore, D.M. and Reynolds, R.C. (1997) *X-ray Diffraction and the Identification and Analysis of Clay Minerals*, 2nd edition. Oxford University Press, New York.

Mustard, R., Baker, T., Brown, V., and Bolt, S. (2003) *Alteration, paragenesis and vein textures, Vera Nancy, Australia*. Economic Geology Research Unit, James Cook University, Australia, contribution **61**, 99–107.

Murphy, D.M.K. (2009) Regolith Expression of Hydrothermal Alteration: A study of the Groundrush and Vera Nancy Gold Deposits of Northern Australia. PhD thesis, The University of Western Australia, 169 pp.

Richards, D.R., Elliot, G.J., and Jones, B.H. (1998) Vera North and Nancy gold deposits, Pajingo. Pp. 685–690 in: *Geology of Australian and Papua New Guinean Mineral Deposits* (D.A. Berkman and D.H. Mackenzie, editors). The Australasian Institute of Mining and Metallurgy, Melbourne.

Rimmer, S.M. and Eberl, D.D. (1982) Origin of an underclay as revealed by vertical variations in mineralogy and chemistry. *Clays and Clay Minerals*, **30**, 422–430.

Robertson, I.D.M. and Eggleton, R.A. (1991) Weathering of granitic muscovite to kaolinite and halloysite and of plagioclase-derived kaolinite to halloysite. *Clays and Clay Minerals*, **39**, 113–126.

Simpson, M.P, Mauk, J.L., and Simmons, S.F. (2001) Hydrothermal alteration and hydrologic evolution of the Golden Cross epithermal Au-Ag deposit, New Zealand. *Economic Geology*, **96**, 773–796.

Środoń, J. and Eberl, D.D. (1984) Illite. Pp. 495–544 in: *Micas* (S.W. Bailey, editor). Reviews in Mineralogy, **13**, Mineralogical Society of America, Washington D.C.

St Pierre, T.G., Singh, B., Webb, J., and Gilkes, R.J. (1992) Mössbauer spectra of soil kaolins from south-western Australia. *Clays and Clay Minerals*, **40**, 341–346.

Stanley, C.R., Baker, T., Mustard, R., Brown, V., Radford, N., and Butler, I. (2003) Lithogeochemistry and hydrothermal alteration at the Pajingo low-sulfidation epithermal gold vein, Drummond Basin, Queensland. P. 55 in: *21st International Geochemical Exploration Symposium, Program with Abstracts*, **21**. Association of Exploration Geochemists, Dublin.

Tillick, D.A., Peacor, D.R., and Mauk, J.L. (2001) Genesis of dioctahedral phyllosilicates during hydrothermal alteration of volcanic rocks: 1. The Golden Cross epithermal ore deposit, New Zealand. *Clays and Clay Minerals*, **49**, 126–140.

Varajão, A.F.D.C., Gilkes, R.J., and Hart, R.D. (2001) The relationship between kaolinite crystal properties and the origin of materials for a Brazilian kaolin deposit. *Clays and Clay Minerals*, **49**, 44–59.

Watanabe, T. (1981) Identification of illite/montmorillonite interstratifications by X-ray powder diffraction. *Journal of the Mineralogical Society of Japan*, Special Issue **15**, 32–41 (in Japanese).

Weaver, C.E., Wampler, J.M., and Pecuil, T.E. (1967) Mössbauer analysis of iron in clay minerals. *Science*, **156**, 504–508.

(*Received 21 March 2010; revised 6 November 2010; Ms. 402; A.E. W.D. Huff*)